Dalton Transactions

Accepted Manuscript

ROYAL SOCIETY OF CHEMISTRY

www.rsc.org/dalton

Graphic abstract

Smaller Ag_2CrO_4 nanoparticles were highly dispersed on the large surface area g-C_3N_4 sheets and exhibited significantly enhanced photocatalytic activity.

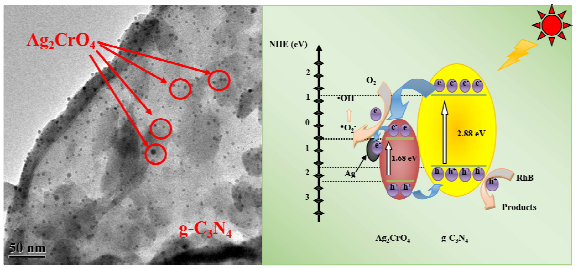

Ag_2CrO_4 nanoparticles loaded on two-dimensional large surface area graphite-like carbon nitride sheets: simple synthesis and excellent photocatalytic performance

Lei Shi [b], Lin Liang [c], Fangxiao Wang [b], Mengshuai Liu [b], Jianmin Sun [a, b] *

a. State Key Laboratory of Urban Water Resource and Environment, Harbin Institute of Technology, Harbin 150080, China

b. The Academy of Fundamental and Interdisciplinary Science, Harbin Institute of Technology, Harbin 150080, China

c. School of Life Science and Technology, Harbin Institute of Technology, Harbin 150080, China

*Corresponding author: Jianmin Sun

E-mail: sunjm@hit.edu.cn

Tel.:+86 451 86403715

Abstract

Graphite-like carbon nitride (g-C_3N_4) with large surface area was prepared through thermal condensation of guanidine hydrochloride at 650 °C, various amounts of silver chromate (Ag_2CrO_4) nanoparticles with small size were highly loaded on the g-C_3N_4 by a simple co-precipitation method at room temperature. The chemical constituent, surface structure and optical properties of the resultant Ag_2CrO_4/g-C_3N_4 composite were thoroughly characterized. And the photocatalytic performances were evaluated by degradation of Rhodamine B (RhB) and phenol, the experimental results indicated that the as-prepared Ag_2CrO_4/g-C_3N_4 composite presented excellent photocatalytic activity under visible-light irradiation. With the mass ratio of Ag_2CrO_4 to g-C_3N_4 at 1:2, the Ag_2CrO_4/g-C_3N_4 composite exhibited the optimal photocatalytic activity for degrading RhB, approximately 6.1 and 10.4 times higher than those on pure g-C_3N_4 and bare Ag_2CrO_4 particles. The improved photocatalytic activity was mainly attributed to the combined effect including the larger surface area, highly dispersed smaller Ag_2CrO_4 nanoparticles, stronger visible absorption and higher charge separation efficiency of the Ag_2CrO_4/g-C_3N_4 composite. Moreover, the possible mechanism for the photocatalytic activity was tentatively proposed.

Keywords: Ag_2CrO_4/g-C_3N_4 photocatalyst; visible light; pollutants degradation; large surface area

1. Introduction

In recent years, photocatalysts with simple synthesis, efficient and sustainable capacity have obtained worldwide attention due to their potential values in energy conversion and environmental purification. [1, 2] Nevertheless, as the most generally researched photocatalyst, TiO_2, owing to its wide band gap, low conversion efficiency for solar energy and the high recombination of photoinduced electron-hole pairs, has been seriously confined for its photocatalytic performance. [3] Recently, a great many of novel visible-light-responsive photocatalysts have been developed, such as CuO, [4] CdS, [5] Bi_2WO_6, [6] and Co_3O_4, [7] etc. Among them, graphite-like carbon nitride (g-C_3N_4) with a narrow band gap of 2.7 eV, as a kind of metal-free semiconductor, has attracted more and more interest due to its excellent photocatalytic performance for water splitting [8-10] and photodegradation of organic pollutants under visible light. [11-13] Nevertheless, the photocatalytic activity of bulk g-C_3N_4 is still restricted because of the low separation rate of the photoinduced electron-hole pairs, the absorbance of only blue light up to 460 nm and its low specific surface area.

Moreover, silver-based photocatalysts have also been confirmed to be a kind of promising catalysts because of their excellent light sensitivity and high photocatalytic activity. Various types of silver-based photocatalysts, such as silver halides, [14-16] Ag_3PO_4, [17] Ag_2CO_3, [18] $AgVO_3$, [19] Ag_2CrO_4 [20] and Ag_2O [21] have exhibited the abilities for degrading the organic pollutants under visible-light irradiation. Among them, Ag_2CrO_4 has been proved a novel high-efficiency visible-light-driven photocatalyst due to its strong absorption in visible-light region, unique electronic structure and

crystal structure. [22] However, similar to other silver-based photocatalysts, the big aggregated particle size and easy photocorrosion property seriously caused poor stability and restricted the photocatalytic performance of Ag_2CrO_4 photocatalyst.

For overcoming the separate shortcomings of g-C_3N_4 and silver-based photocatalysts to develop promising photocatalytic materials, researchers have coupled g-C_3N_4 with several silver-based photocatalysts, including Ag/g-C_3N_4, [23, 24] g-C_3N_4/Ag_2O, [25, 26] Ag/AgX/g-C_3N_4, [27-29] g-C_3N_4/Ag_3PO_4 [30] and g-C_3N_4/Ag_2CO_3, [31] which could not only decrease the recombination rates of photogenerated electron-hole pairs and enhance the visible-light absorption of g-C_3N_4, but also reduce the size and photocorrosion of silver-based photocatalysts to promote their stability. Satisfactorily, the excellent photocatalytic capacities were obtained. Nevertheless, for the previous composites constituted with g-C_3N_4 and silver-based photocatalysts, low surface area bulk g-C_3N_4 (<10 m^2 g^{-1}) was usually used as support so that the further improvement of photocatalytic activity was restricted. In this work, two-dimensional g-C_3N_4 sheets with large surface area were produced through simple thermal condensation of guanidine hydrochloride, then Ag_2CrO_4/g-C_3N_4 composite was prepared via a facile co-precipitation method using $AgNO_3$ and K_2CrO_4 as Ag^+ and CrO_4^{2-} sources. Ag_2CrO_4 nanoparticles with the smaller sizes of 2-5 nm were uniformly loaded on the surface of 2D g-C_3N_4 sheets. Compared with the bare Ag_2CrO_4 and g-C_3N_4, the as-prepared Ag_2CrO_4/g-C_3N_4 composite displayed more excellent visible-light photocatalytic performance for degrading RhB dye and phenol. The reusability of the photocatalyst was evaluated by five consecutive catalytic runs,

moreover, based on the experimental results, the probable photocatalytic reaction mechanism was also proposed.

2. Experimental

2.1 Synthesis of Ag_2CrO_4/g-C_3N_4 composite

The 2D g-C_3N_4 with large surface area was synthesized according to the previous report. [32] In a typical run, 4 g guanidine hydrochloride was placed in a crucible with a cover, then the crucible was heated to 650 °C for 3 h at a heating rate of 3 °C min^{-1}, finally, the crucible was cooled to room temperature. The obtained products were collected and ground into powder.

Ag_2CrO_4/g-C_3N_4 composite was prepared by the co-precipitation method. The formation process for the Ag_2CrO_4 loaded on the g-C_3N_4 surface was proposed in Scheme 1. Typically, 0.051 g $AgNO_3$ and 0.100 g g-C_3N_4 were added into 40 mL distilled water. After ultrasonic treatment for 60 min to ensure Ag^+ fully adsorbed on the surface of g-C_3N_4 sheets, 20 mL solution containing 0.029 g K_2CrO_4 was dropped slowly into the above mixture and kept stirring for 2 h at room temperature, the resultant pale brick-red precipitate was filtered, washed with distilled water and ethanol, and then dried in oven at 60 °C for 12 h. Finally, the Ag_2CrO_4/g-C_3N_4 composite with theoretical weight ratio Ag_2CrO_4 to g-C_3N_4 at 1:2 was prepared and named as Ag_2CrO_4/g-C_3N_4-2. Accordingly, the Ag_2CrO_4/g-C_3N_4 composites with weight ratios of 1:1 and 1:4 were obtained through changing the amounts of $AgNO_3$ and K_2CrO_4, and denoted as Ag_2CrO_4/g-C_3N_4-1 and Ag_2CrO_4/g-C_3N_4-3, respectively.

The pure Ag_2CrO_4 was synthesized by the same method only in the absence of g-C_3N_4.

(Scheme 1)

2.2 Characterizations

The X-ray diffraction (XRD) patterns were carried out on a Bruker D8 Advance X-ray powder diffractometer with Cu Kα radiation (40 kV, 30 mA) for phase identification. XPS measurements were recorded on Thermo Fisher Scientific Escalab 250Xi. The transmission electron microscope (TEM) was investigated by FEI Tecnai G2 microscope and scanning transmission electron microscope (STEM) images were obtained by FEI Tecnai G2 F20 microscope. The Brunauer-Emmett-Teller (BET) surface areas were collected at -196 °C using a Micromeritics Tristar 3020 analyzer, samples were outgassed at 120 °C for 12 h prior to the measurements. The UV-vis diffuse reflectance spectra (DRS) were obtained by a Perkin Elmer Lambda 750 UV-vis spectrometer. The photoluminescence spectra (PL) of samples were measured by a Perkin Elmer LS55 spectrometer with the excitation wavelength of 325 nm.

2.3 Photocatalytic test

The photocatalytic performances of the sample were evaluated through degradation of RhB and phenol solution under visible-light irradiation. 25 mg photocatalyst was dispersed into 50 mL 5 mg L^{-1} RhB or phenol solution under magnetic stirring. Prior to the light irradiation, the dispersion was kept in dark for 60

min under stirring to reach the adsorption-desorption equilibrium. A 300 W Xe lamp with cut off filter ($\lambda > 400$ nm) provided visible-light source. After irradiation, 4 mL solution was collected at given time interval and separated the catalyst by centrifugation, then analyzed on UV-vis spectrometer. The concentration of phenol was detected through colorimetric method using 4-aminoantipyrine as the colour-developing agent at the wavelength of 510 nm. [33, 34] For comparison, photocatalytic reactions were also investigated in the presence of pure g-C_3N_4, bare Ag_2CrO_4 and in the absence of any catalyst. The degradation efficiency was calculated by C/C_0, where C is the concentration of remaining pollutant solution at each time interval, while C_0 is the initial concentration.

3. Results and Discussion

The typical XRD patterns of pure g-C_3N_4, Ag_2CrO_4 and Ag_2CrO_4/g-C_3N_4-2 composite were shown Fig. 1. For g-C_3N_4, two diffraction peaks at 27.6° and 13.0° were indexed to (002) and (100) planes of hexagonal g-C_3N_4 (JCPDS card no. 87-1526), corresponding to the graphite-like stacking and in-plane structural repeating motifs of the conjugated aromatic units of g-C_3N_4. [35] In the Ag_2CrO_4 sample, all diffraction peaks were attributed to the orthorhombic phase of Ag_2CrO_4 (JCPDS No. 26-0952). [34] For Ag_2CrO_4/g-C_3N_4 composite, orthorhombic phase Ag_2CrO_4 and hexagonal phase g-C_3N_4 were both observed and no other impurity peaks were found, indicating that Ag_2CrO_4 and g-C_3N_4 existed in the Ag_2CrO_4/g-C_3N_4 composite.

(**Fig. 1)**

The surface structures of the pristine g-C_3N_4, Ag_2CrO_4, and Ag_2CrO_4/g-C_3N_4-2 composite were investigated using XPS analyses in Fig. 2. Compared with pure g-C_3N_4 and Ag_2CrO_4, all the peaks ascribed to Ag, Cr, O, C and N elements were displayed in the Ag_2CrO_4/g-C_3N_4 sample (Fig. 2A). Fig. 2B-F showed the corresponding high-resolution XPS spectra of each element. The two individual peaks with the binding energies of 368.0 and 374.0 eV in Fig. 2B were assigned to Ag^+ $3d_{5/2}$ and Ag^+ $3d_{3/2}$, respectively. [36] The peak at 573.5 eV in Fig. 3C was Cr 2p spectrum. The O 1s high resolution XPS spectrum could be split into two peaks: the peak at 532.8 eV was attributed to the external -OH group or water species adsorbed on the surface of the sample, the other peak at 531.2 eV corresponded to the oxygen in Ag_2CrO_4. Moreover, C 1s spectrum exhibited two main peaks at 284.6 and 278.8 eV. The peak at 284.6 eV was assigned to carbon atoms in a pure carbonaceous environment, the other peak could be identified as the sp^2 C atoms bonded in N–C=N coordinations of g-C_3N_4. [37] Besides, N 1s XPS spectrum in Fig. 3F was deconvoluted into four peaks with binding energies of 398.6, 399.7, 400.9 and 404.6 eV. The peaks at 398.6, 399.7 and 400.9 eV were typically attributed to sp^2-bonded N atom to two carbon atoms (C−N=C), tertiary nitrogen (N−$(C)_3$) and amino functional groups with hydrogen atom (N−H), respectively. [38, 39] The peak at 404.6 eV was caused by the positive charge localization in heterocycles.[40, 41] XPS results also revealed the composite was consisted of Ag_2CrO_4 and g-C_3N_4.

(**Fig. 2**)

In order to observe the morphology of the bare g-C_3N_4, Ag_2CrO_4 and as-prepared

Ag_2CrO_4/g-C_3N_4-2 composite, TEM was provided in Fig. 3. The pure g-C_3N_4 sample possessed very thin 2D layer structure and some abundant pores evenly dispersed on the surface, which were attributed to the generated NH_3 as the bubble templates during the formation process of g-C_3N_4 using guanidine hydrochloride precursor. [32] And as for pristine Ag_2CrO_4 sample in Fig. 3B, besides the obvious aggregations there was no special morphological feature, and the sizes of Ag_2CrO_4 particles were large at around 200 nm. TEM images of Ag_2CrO_4/g-C_3N_4-2 composite indicated that smaller 2-5 nm of Ag_2CrO_4 nanoparticles were uniformly embedded on the g-C_3N_4 (labeled by red circles in Fig. 3C and D). STEM images of Ag_2CrO_4/g-C_3N_4-2 composite also verified that small Ag_2CrO_4 nanoparticles evenly dispersed on the porous g-C_3N_4.

(**Fig. 3**)

The surface areas of as-prepared g-C_3N_4 and Ag_2CrO_4/g-C_3N_4 samples were also provided, for the parent g-C_3N_4, the BET surface area was 65 m^2 g^{-1}. After decorations with Ag_2CrO_4 nanoparticles, the BET surface areas of Ag_2CrO_4/g-C_3N_4-1, Ag_2CrO_4/g-C_3N_4-2 and Ag_2CrO_4/g-C_3N_4-3 were decreased respectively to 33.5, 40.0 and 55.0 m^2 g^{-1}. The BET surface areas of Ag_2CrO_4/g-C_3N_4 composites were reduced, which was caused by some aggregations of Ag_2CrO_4 nanoparticles with loading amounts increasing. But still attractively, their surface areas were much higher than bulk g-C_3N_4. The large surface area would supply more reactive sites, contributing to improve the photocatalytic activity.

UV-vis DRS was used to investigate the Ag_2CrO_4 effect on the optical properties of g-C_3N_4 in the visible range. As presented in Fig. 4, pure g-C_3N_4 and Ag_2CrO_4 both

exhibited photoabsorptions from ultraviolet to visible light, which were related to the photocatalytic activities [32, 22]. Moreover, their separate band absorption edge was around 430 and 738 nm, corresponding to the band gap at 2.88 and 1.68 eV. For Ag_2CrO_4/g-C_3N_4-2 composite, more intense absorption in the range of 200-800 nm was harvest than g-C_3N_4, and the wavelength thresholds of the Ag_2CrO_4/g-C_3N_4-2 composite were estimated at 546 and 710 nm, corresponding to the band gap at 2.27 and 1.74 eV, respectively ascribed to g-C_3N_4 and Ag_2CrO_4. The reduced band gaps of the Ag_2CrO_4/g-C_3N_4-2 composite and more responsive to the visible light were caused by the loaded Ag_2CrO_4 nanoparticles, thus more efficient utilization of solar energy could be achieved, and the improved photocatalytic activity of Ag_2CrO_4/g-C_3N_4 composite would be anticipated.

(Fig. 4)

As the separation of photogenerated electrons-holes is another key factor for the efficient photocatalytic activity, the evidence for the separation efficiency was proved by photoluminescence spectra, which is extensively applied for detecting the separation, transfer and recombination processes of the photoinduced electron-hole pairs on a semiconductor. Since PL spectra emission derives from the recombination of free carriers, it is generally believed that a weaker PL intensity means a higher separation probability of photogenerated charge carriers. Fig. 5 presented PL spectra of bare g-C_3N_4 and Ag_2CrO_4/g-C_3N_4 composites at an excitation wavelength of 325 nm. It was clearly found that PL emission intensity of pure g-C_3N_4 was much stronger than those of Ag_2CrO_4/g-C_3N_4 composites, indicating that photoinduced electron-hole

pairs could be efficiently separated through the heterojunctions between Ag_2CrO_4 and g-C_3N_4, additionally, the spacious pores of g-C_3N_4 also favored the transfer of photogenerated charges.

(Fig. 5)

The photocatalytic capacities of the as-prepared samples were evaluated through degrading RhB and phenol under visible light. As shown in Fig. 6A, it was obviously observed that photodegradation was not occurred without catalyst after visible-light irradiation, meaning that the photolysis of RhB could be ignored. Excitingly, the Ag_2CrO_4/g-C_3N_4 composites showed more excellent photocatalytic activities than pristine Ag_2CrO_4 and g-C_3N_4, and their photocatalytic activities depended on the mass ratio of Ag_2CrO_4 and g-C_3N_4, the as-prepared Ag_2CrO_4/g-C_3N_4-2 composite exhibited the highest activity. The above results indicated that the loading amount of Ag_2CrO_4 was crucial to the synergistic effects between the two components. Moreover, to have a better understanding of the reaction kinetics of the RhB degradation catalyzed by various samples, Fig. 6B showed the relationships between ln (C_0/C) and irradiation time. As all the relationships were linear ($R > 0.99$), the photocatalytic degradation curves fit well with first-order reactions. And correspondingly, the rate constants of Ag_2CrO_4/g-C_3N_4-1, Ag_2CrO_4/g-C_3N_4-2 and Ag_2CrO_4/g-C_3N_4-3 were 0.1886, 0.5783 and 0.4908 min^{-1} (Fig. 6C). The Ag_2CrO_4/g-C_3N_4-2 composite possessed the highest rate constant, which was approximately 6.1 times larger than g-C_3N_4 (0.0941 min^{-1}) and 10.4 times larger than pure Ag_2CrO_4 (0.0551 min^{-1}). In addition, for excluding the effect of dye self-sensitization, the photodegradation of phenol was further conducted.

As presented in Fig. 6D, Ag_2CrO_4/g-C_3N_4-2 composite exhibited better photocatalytic efficiency at 75.0%, much higher than 35.2% over the bare g-C_3N_4 and 44.1% over pristine Ag_2CrO_4 under the same conditions. Then the reaction kinetics of the phenol photodegradation and the corresponding rate constants were shown in Fig. 6E-F. Clearly, the photocatalytic degradation curves of phenol fit well with first-order reactions, and the rate constants of Ag_2CrO_4/g-C_3N_4-2 composite (0.0229 min^{-1}) was approximately 3 times larger than g-C_3N_4 (0.0077 min^{-1}) and twice as large as pure Ag_2CrO_4 (0.0111 min^{-1}). The improved photocatalytic activities were attributed to the combined effects including larger surface area, highly dispersed smaller Ag_2CrO_4 nanoparticles, stronger visible absorption and higher charge separation efficiency in the Ag_2CrO_4/g-C_3N_4 composite.

(Fig. 6)

In the photodegradation process, some active species including electrons (e^-), holes (h^+), superoxide radicals ($\bullet O_2^-$) and hydroxyl radicals ($\bullet$OH) were formed under light irradiation. In order to detect the main reactive species for the photodegradation over Ag_2CrO_4/g-C_3N_4 composite and discuss the reaction mechanism, the control experiments of quenching active species were conducted in the photodegadation of RhB. Herein, tert-butyl alcohol (t-BuOH) was used to quench $\bullet$OH, [42, 43] p-benzoquinone (p-BQ) as $\bullet O_2^-$ scavenger [44] and ammonium oxalate (AO) as h^+ quencher. [11] Fig. 7 displayed the effects of different scavengers on the degradation performances. The addition of t-BuOH had slight effect on the activities, which implied that $\bullet$OH made small contributions to the photocatalytic reaction. And

adding AO played a medium role in the degradation of RhB, indicating h^+ played an important role in the photocatalytic process. And the degradation rate displayed significant decrease in the presence of p-BQ, the degradation efficiency kept only 25% after p-BQ addition, suggesting that $\bullet O_2^-$ radical were the predominant active species in the photodegradation of RhB.

(Fig. 7)

From the viewpoint of practical applications, the stability of photocatalytic activity over Ag_2CrO_4/g-C_3N_4 composite was also investigated. After each run, the catalyst was collected and washed with ethanol then reused for the next run. As presented in Fig. 8, although the catalytic activity exhibited a certain extent reduction after 5 recycles, the spent Ag_2CrO_4/g-C_3N_4 composite still possessed enhanced photocatalytic performance compared with pure g-C_3N_4 and Ag_2CrO_4. The loss of photocatalytic activity might be attributed to the following factors. Firstly, some Ag_2CrO_4 nanoparticles gradually agglomerated (labeled by red circles) on g-C_3N_4 surface during the photocatalytic reaction process, as shown in Fig. 9A, compared with the fresh sample, the Ag_2CrO_4 nanoparticles after reaction became bigger (5-10 nm), which would have a negative effect on the photocatalytic performance. [45] Moreover, due to the agglomerations Ag_2CrO_4 nanoparticles during the photocatalytic reaction, more space of the g-C_3N_4 surface was exposed, leading to the peak intensities of g-C_3N_4 in the spent Ag_2CrO_4/g-C_3N_4-2 composite were much stronger than the fresh composite (Fig. 9B). Secondly, metallic Ag at 38.8° was observed in the XRD pattern of the spent Ag_2CrO_4/g-C_3N_4 composite, suggesting a small fraction of

Ag^+ in Ag_2CrO_4 were reduced to metal Ag^0 by photogenerated electrons. [22] Furthermore, in order to support the existence of metallic Ag, Ag 3d XPS spectra after photocatalytic reaction were conducted in Fig. 10. Compared with the fresh Ag_2CrO_4/g-C_3N_4 composite, Ag 3d peaks of the spent catalyst could be further divided into two different peaks, the peaks at 368.0 eV and 374.0 eV were assigned to Ag(I) of Ag_2CrO_4, and the peaks at 368.9 eV and 374.9 eV were attributed to metallic Ag(0).[26] As we all known, Ag is a good electron acceptor, which could capture some electrons from the CB of Ag_2CrO_4, contributing to the photoexcited carriers transfer. However, more Ag could enrich more electrons, which in principle could react with oxygen via multi-electron-transfer processes ($O_2 + 2e^- + 2H^+ = H_2O_2$; $O_2 + 4e^- + 4H^+ = 2H_2O$), [25] which resulted in the amounts of e^- for the formation of main active species $\bullet O_2^-$ decrease. Additionally, the excessive Ag^0 could also become the recombination centers for electrons and holes, causing that quantum efficiency reduced. [46]

(Fig. 8)

(Fig. 9)

(Fig. 10)

In order to further explain the photocatalytic reaction mechanism of Ag_2CrO_4/g-C_3N_4 composite, the conduction band (CB) and the valence band (VB) positions of g-C_3N_4 and Ag_2CrO_4 were determined by the following equations: [22, 47, 48]

$$E_{VB} = X - E^e + 0.5\ Eg \quad (1)$$

$$E_{CB} = E_{VB} - Eg \quad (2)$$

where E_{VB} is the valence band edge potential, E_{CB} is the conduction band edge potential, X is the electronegativity of the semiconductor, which is the geometric mean of the electronegativity of the constituent atoms, E^e is the energy of free electrons on the hydrogen scale at about 4.5 eV, Eg is the band gap energy of the semiconductor. Based on the band gap, the CB and VB edge potentials of Ag_2CrO_4 were respectively determined at 0.52 and +2.20 eV, and those of g-C_3N_4 were calculated at -1.21 and +1.67 eV.

Hence, based on the above experimental results and physicochemical properties of g-C_3N_4 and Ag_2CrO_4, a possible photocatalytic mechanism of Ag_2CrO_4/g-C_3N_4 composite was proposed. When the composite was irradiated by visible light, electrons (e^-) and holes (h^+) were excited on the conduction bands and the valence bands of g-C_3N_4 and Ag_2CrO_4. Photoexcited carriers could transfer smoothly due to the matching potentials of the composites, as shown in Fig. 11. g-C_3N_4 had a more negative potential of the CB (E_{CB}= -1.21 eV) than that of Ag_2CrO_4 (E_{CB}= + 0.52 eV). Therefore, the excited electrons on g-C_3N_4 could directly be injected into the CB of Ag_2CrO_4. Then the partial Ag^+ in Ag_2CrO_4 were reduced by photogenerated electrons to form metallic Ag, [22] which worked as electron pools and captured the photogenerated electrons from Ag_2CrO_4. The enriched electrons on the CB of Ag_2CrO_4 and the surface of Ag reacted with oxygen to generate $\bullet O_2^-$. And $\bullet O_2^-$ radicals combined with H_2O to further transform into $\bullet$OH. Meanwhile, h^+ could transfer from the VB of Ag_2CrO_4 (+ 2.20 eV) to g-C_3N_4 (+ 1.67 eV), which promoted the efficient separation of photoinduced electrons and holes. And their E_{VB} were lower

than the standard redox potential of $\bullet OH/H_2O$ (2.68 eV), [30] indicating that the photogenerated h^+ could not oxidize H_2O to $\bullet OH$. Therefore, h^+ would directly react with RhB. These reactive species of h^+, $\bullet O_2^-$ and $\bullet OH$ were responsible for the degradation of organic pollutant. Simultaneously, photogenerated electrons and holes were easily separated in the transfer process, enhancing quantum efficiency greatly.

(Fig. 11)

4. Conclusion

The novel large surface area 2D g-C_3N_4 sheets loaded with highly dispersed Ag_2CrO_4 nanoparticles with smaller sizes have been facilely fabricated. Under the visible-light irradiation, the Ag_2CrO_4/g-C_3N_4 composite exhibited more superior photocatalytic performance for degrading RhB and phenol than bare g-C_3N_4 and Ag_2CrO_4 particles. The enhanced photocatalytic activity of the Ag_2CrO_4/g-C_3N_4 composite is derived from the synergistic effects including the larger surface area, stronger visible absorption and higher charge separation efficiency of photoinduced electron-hole pairs. The Ag_2CrO_4/g-C_3N_4 composite may serve as a promising candidate catalyst widely applied in pollution treatment applications.

Acknowledgements

We sincerely acknowledge the financial supports from National Natural Science Foundation of China (21373069), Science Foundation of Harbin City (NJ20140037), State Key Lab of Urban Water Resource and Environment of Harbin Institute of

Technology (HIT2015DX08) and the Fundamental Research Funds for the Central Universities (HIT. IBRSEM. 201327).

References

1. M. R. Hoffmann, S. T. Martin, W. Choi and D. W. Bahnemann, *Chem. Rev.*, 1995, **95**, 69-96.
2. H. Wang, L. Zhang, Z. Chen, J. Hu, S. Li, Z. Wang, J. Liu and X. Wang, *Chem. Soc. Rev.*, 2014, **43**, 5234-5244.
3. X. B. Chen and S. S. Mao, *Chem. Rev.*, 2007, **107**, 2891-2959.
4. S. Liu, J. Tian, L. Wang, Y. Luo and X. Sun, *Catal. Sci. Technol.*, 2012, **2**, 339-344.
5. N. Z. Bao, L. M. Shen, T. Takata and K. Domen, *Chem. Mater.*, 2008, **20**, 110-117.
6. H. Fu, C. Pan, W. Yao and Y. Zhu, *J. Phys. Chem. B*, 2005, **109**, 22432-22439.
7. A. Gasparotto, D. Barreca, D. Bekermann, A. Devi, R. A. Fischer, P. Fornasiero, V. Gombac, O. I. Lebedev, C. Maccato, T. Montini, G. V. Tendeloo and E. Tondello, *J. Am. Chem. Soc.*, 2011, **133**, 19362-19365.
8. X. C. Wang, K. Maeda, A. Thomas, K. Takanabe, G. Xin, J. M. Carlsson, K. Domenet and M. Antonietti, *Nat. Mater.*, 2009, **8**, 76-80.
9. S. Yin, J. Han, T. Zhou and R. Xu, *Catal. Sci. Technol.*, 2015, **5**, 5048-5061.
10. Z. Zhao, Y. Sun and F. Dong, *Nanoscale*, 2015, **7**, 15-37.

11. L. Shi, L. Liang, J. Ma, F. X. Wang and J. M. Sun, *Dalton Trans.*, 2014, **43**, 7236-7244.

12. S. C. Lee, H. O. Lintang and L. Yuliati, *Chem. Asian J.*, 2012, **7**, 2139-2144.

13. M. Tahir, C. Cao, F. K. Butt, S. Butt, F. Idrees, Z. Ali, I. Aslam, M. Tanveer, A. Mahmood and N. Mahmood, *CrystEngComm*, 2014, **16**, 1825-1830.

14. P. Wang, B. Huang, X. Qin, X. Zhang, Y. Dai, J. Wei and M. Whangbo, *Angew. Chem. Int. Ed.*, 2008, **47**, 7931-7933.

15. D. Wang, Y. Duan, Q. Luo, X. Li and L. Bao, *Desalination*, 2011, **270**, 174-180.

16. H. Yu, L. Liu, X. Wang, P. Wang, J. Yu and Y. Wang, *Dalton Trans.*, 2012, **41**, 10405-10411.

17. Y. Bi, S. Ouyang, N. Umezawa, J. Cao and J. Ye, *J. Am. Chem. Soc.*, 2011, **133**, 6490-6492.

18. H. Dong, G. Chen, J. Sun, C. Li, Y. Yu and D. Chen, *Appl. Catal. B: Environ.*, 2013, **134-135**, 46-54.

19. W. Zhao, Y. Guo, Y. Faiz, W. T. Yuan, C. Sun, S. M. Wang, Y. H. Deng, Y. Zhuang, Y. Li, X. M. Wang, H. He and S. G. Yang, *Appl. Catal. B: Environ.*, 2015, **163**, 288-297.

20. Y. Liu, H. Yu, M. Cai and J. Sun, *Catal. Commun.*, 2012, **26**, 63-67.

21. X. Wang, S. Li, H. Yu, J. Yu and S. Liu, *Chem. Eur. J.*, 2011, **17**, 7777-7780.

22. D. Xu, S. Cao, J. Zhang, B. Cheng and J. Yu, *Beilstein J. Nanotechnol.*, 2014, **5**, 658-666.

23. L. Ge, C. Han, J. Liu and Y. Li, *Appl. Catal. A: Gen.*, 2011, **409-410**, 215-222.

24. Y. Yang, Y. Guo, F. Liu, X. Yuan, Y. Guo, S. Zhang, W. Guo and M. Huo, *Appl. Catal. B: Environ.*, 2013, **142-143**, 828-837.

25. M. Xu, L. Han and S. Dong, *ACS Appl. Mater. Interfaces*, 2013, **5**, 12533-12540.

26. L. Shi, L. Liang, J. Ma, F. X. Wang and J. M. Sun, *Catal. Sci. Technol.*, 2014, **4**, 758-765.

27. S. Zhang, J. Li, X. Wang, Y. Huang, M. Zeng and J. Xu, *ACS Appl. Mater. Interfaces*, 2014, **6**, 22116-22125.

28. Y. Yang, W. Guo, Y. N. Guo, Y. Zhao, X. Yuan and Y. H. Guo, *J. Hazard. Mater.*, 2014, **271**, 150-159.

29. H. Xu, J. Yan, Y. Xu, Y. Song, H. Li, J. Xia and C. Huang, *Appl. Catal. B: Environ.*, 2013, **129**, 182-193.

30. S. Kumar, T. Surendar, A. Baruah and V. Shanker, *J. Mater. Chem. A*, 2013, **1**, 5333-5340.

31. Y. Li, L. Fang, R. Jin, Y. Yang, X. Fang, Y. Xing and S. Song, *Nanoscale*, 2015, **7**, 758-764.

32. L. Shi, L. Liang, F. X. Wang, J. Ma and J. M. Sun, *Catal. Sci. Technol.*, 2014, **4**, 3235-3243.

33. X. T. Hong, Z. P. Wang, W. M. Cai, F. Lu, J. Zhang, Y. Z. Yang, N. Ma and Y. J. Liu, *Chem. Mater.*, 2005, **17**, 1548-1552.

34. D. Xu, B. Cheng, S. Cao and J. Yu, *Appl. Catal. B: Environ.*, 2015, **164**, 380-388.

35. F. Dong, Z. Zhao, T. Xiong, Z. Ni, W. Zhang, Y. Sun, and W. K. Ho, *ACS Appl. Mater. Interfaces* 2013, **5**, 11392-11401.

36. H. Yu, R. Liu, X. Wang, P. Wang and J. Yu, *Appl. Catal. B: Environ.* 2012, **111-112**, 326-333.

37. S. Cao, J. Low, J. Yu and M. Jaroniec, *Adv. Mater.*, 2015, **27**, 2150-2176.

38. Q. Xiang, J. Yu and M. Jaroniec, *J. Phys. Chem. C*, 2011, **115**, 7355-7363.

39. J. Zhang, M. Zhang, C. Yang and X. C. Wang, *Adv. Mater.*, 2014, **26**, 4121-4126.

40. J. Zhang, M. Zhang, R. Q. Sun and X. C. Wang, *Angew. Chem. Int. Ed.*, 2012, **51**, 1014-10149.

41. L. Shi, L. Liang, F. X. Wang, M. S. Liu, K. L. Chen, K. N. Sun, N. Q. Zhang and J. M. Sun, *ACS Sustainable Chem. Eng.* 2015, **3**, 3412-3419.

42. X. Bai, R. Zong, C. Li, D. Liu, Y. Liu and Y. F. Zhu, *Appl. Catal. B: Environ.*, 2014, **147**, 82-91.

43. H. Lee and W. Choi, *Environ. Sci. Technol.*, 2002, **36**, 3872-3878.

44. X. Yang, J. Qin, Y. Jiang, R. Li, Y. Li and H. Tang, *RSC Adv.*, 2014, **4**, 18627-18636.

45. H. Xu, Y. X. Song, Y. H. Song, J. X. Zhu, T. T. Zhu, C. B. Liu, D. X. Zhao, Q. Zhang and H. M. Li, *RSC Adv.*, 2014, **4**, 34539-34547.

46. R. Georgekutty, M. K. Seery and S. C. Pillai, *J. Phys. Chem. C*, 2008, **112**, 13563-13570.

47. W. Zhang, Y. Sun, F. Dong, W. Zhang, S. Duan and Q. Zhang, *Dalton Trans.*, 2014, **43**, 12026-12036.

48. L. Shi, L. Liang, F. X. Wang, M. S. Liu and J. M. Sun, *RSC Adv.*, 2015, **5**, 101843-101849.

Figure Captions

Scheme 1 Schematic diagram for the fabrication of Ag_2CrO_4/g-C_3N_4 composite.

Fig. 1 XRD patterns of (a) g-C_3N_4, (b) Ag_2CrO_4 and (c) Ag_2CrO_4/g-C_3N_4-2 composite.

Fig. 2 (A) XPS survey spectra of (a) g-C_3N_4, (b) Ag_2CrO_4 and (c) Ag_2CrO_4/g-C_3N_4-2 composite. The corresponding high-resolution XPS spectra of Ag_2CrO_4/g-C_3N_4-2 composite: (B) Ag 3d, (C) Cr 2p, (D) O 1s, (E) C 1s and (F) N 1s.

Fig. 3 TEM images of (A) g-C_3N_4 and (B) Ag_2CrO_4, (C-D) Ag_2CrO_4/g-C_3N_4-2 composite; (E-F) STEM images for Ag_2CrO_4/g-C_3N_4-2 composite.

Fig. 4 UV-vis absorption spectra of (a) g-C_3N_4, (b) Ag_2CrO_4 and (c) Ag_2CrO_4/g-C_3N_4-2 composite.

Fig. 5 Photoluminescence spectra of (a) pure g-C_3N_4, (b) Ag_2CrO_4/g-C_3N_4-1 (c) Ag_2CrO_4/g-C_3N_4-2 and (d) Ag_2CrO_4/g-C_3N_4-3.

Fig. 6 (A) Degradation rates of RhB, (B) first-order kinetic plots of various samples for degrading RhB, (C) the corresponding rate constants, (D) degradation rates of phenol, (E) first-order kinetic plots for photodegrading phenol and (F) the relevant rate constants. (a) pure g-C_3N_4, (b) Ag_2CrO_4, (c) Ag_2CrO_4/g-C_3N_4-1, (d) Ag_2CrO_4/g-C_3N_4-2, (e) Ag_2CrO_4/g-C_3N_4-3 and (f) without any catalyst.

Fig. 7 Effects of the addition of different scavengers on the degradation of RhB over Ag_2CrO_4/g-C_3N_4-2 composite: (a) no scavenger, (b) adding 1 mM AO, (c) adding 1 mM p-BQ and (d) adding 5 mM t-BuOH.

Fig. 8 Recycling runs in the photodegradation of RhB over Ag_2CrO_4/g-C_3N_4-2 composite.

Fig. 9 (A) TEM image of spent Ag_2CrO_4/g-C_3N_4-2 composite and (B) XRD patterns of the fresh and spent Ag_2CrO_4/g-C_3N_4-2 composite after photocatalytic reaction.

Fig. 10 Ag 3d XPS spectra (a) before and (b) after photocatalytic reaction.

Fig. 11 Proposed photodegradation mechanism of RhB over Ag_2CrO_4/g-C_3N_4 composite.

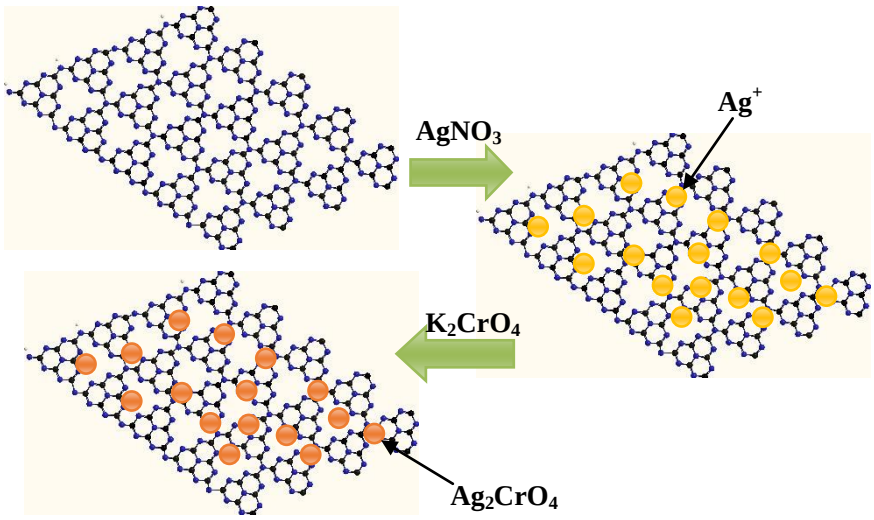

Scheme 1

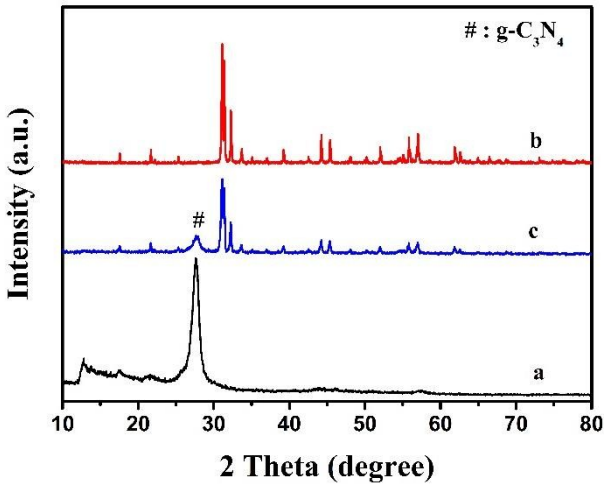

Fig. 1

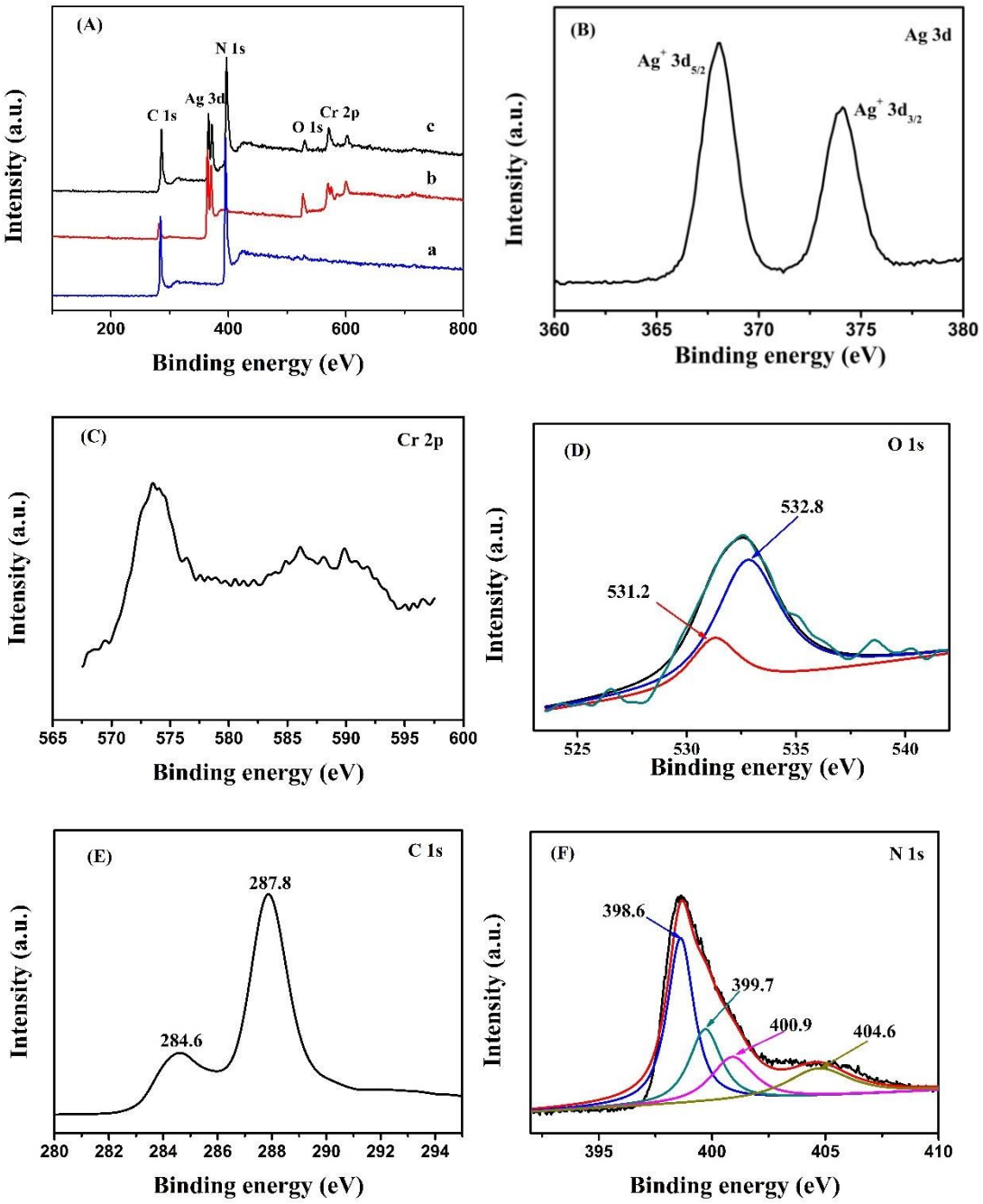

Fig. 2

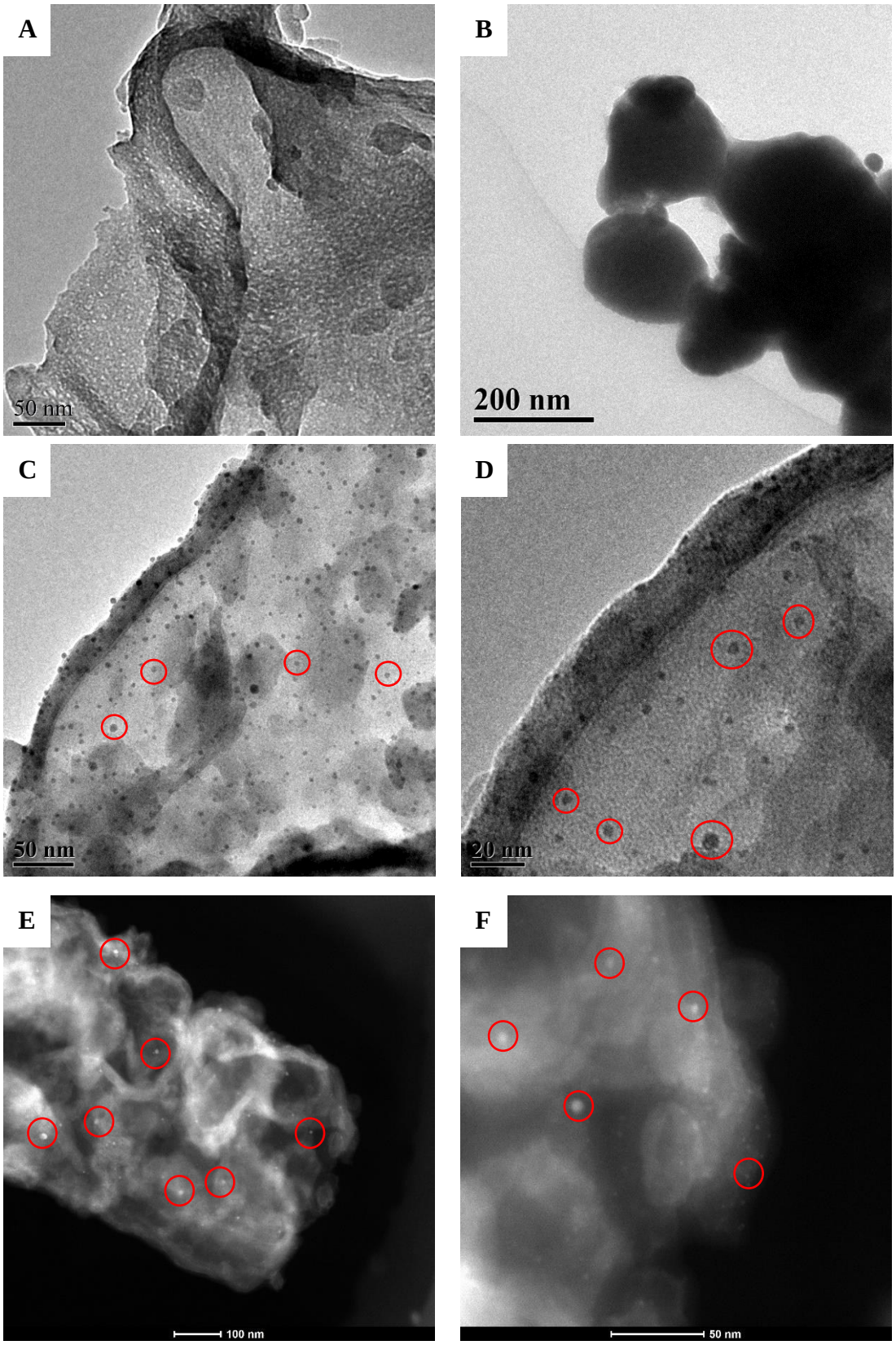

Fig. 3

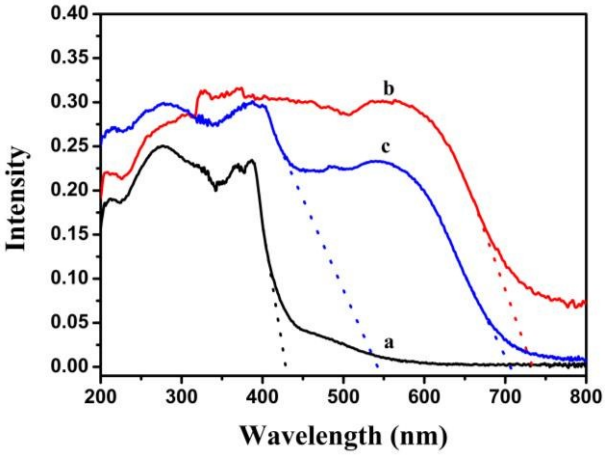

Fig. 4

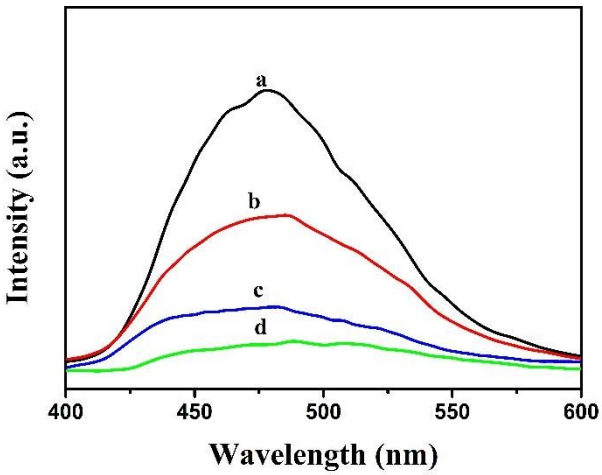

Fig. 5

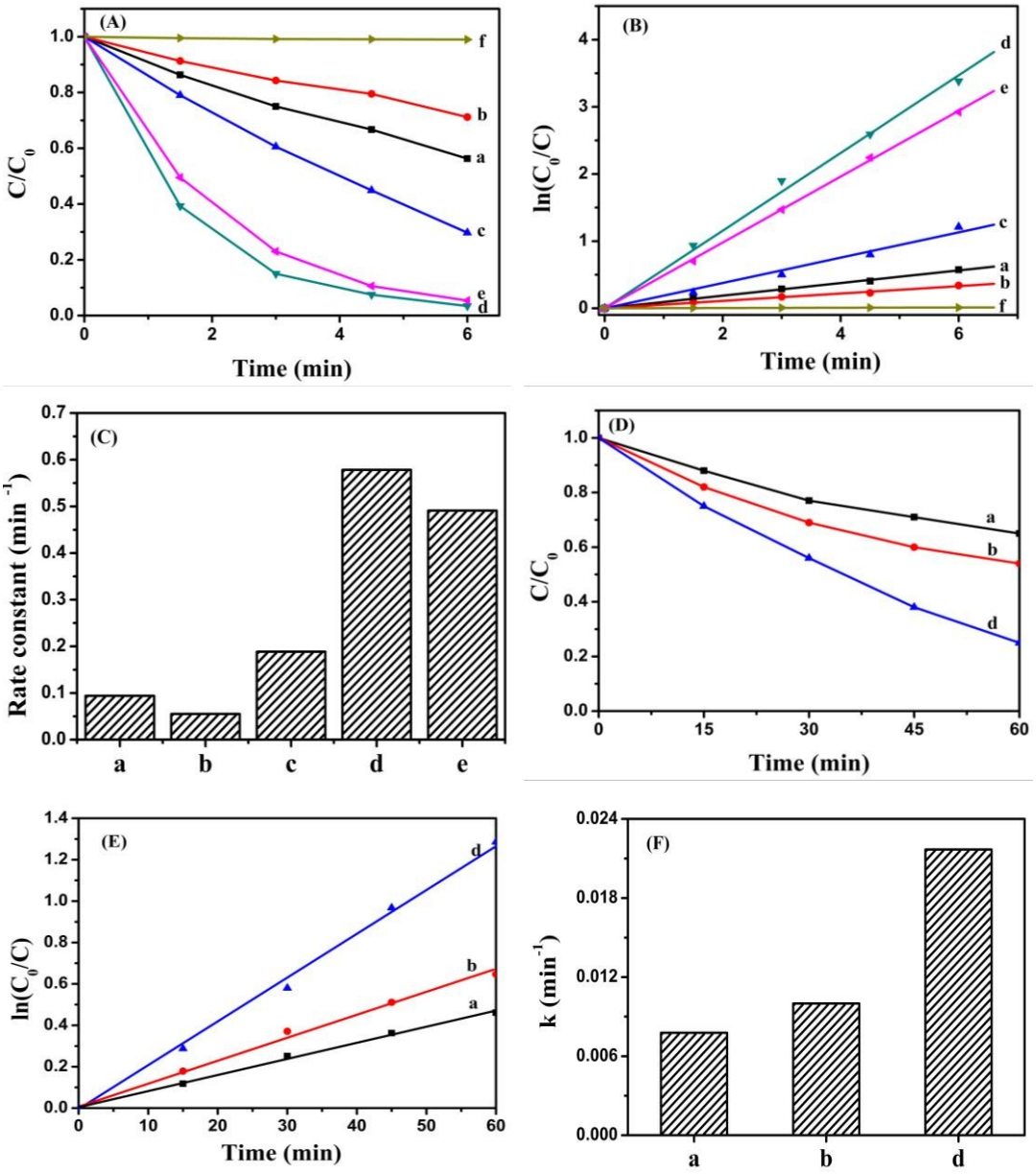

Fig. 6

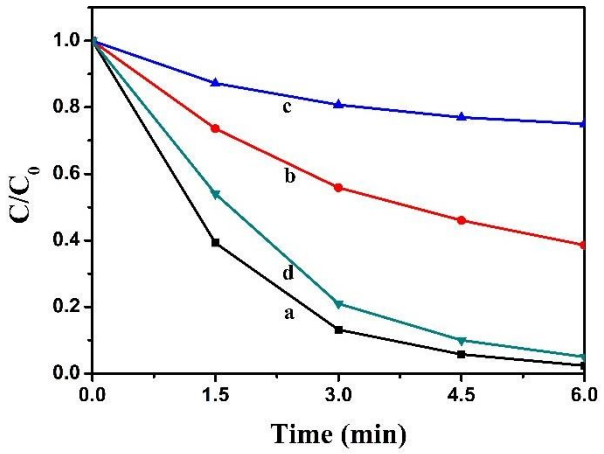

Fig. 7

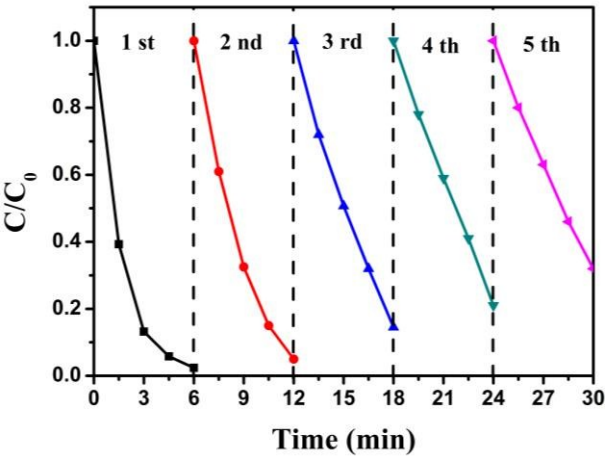

Fig. 8

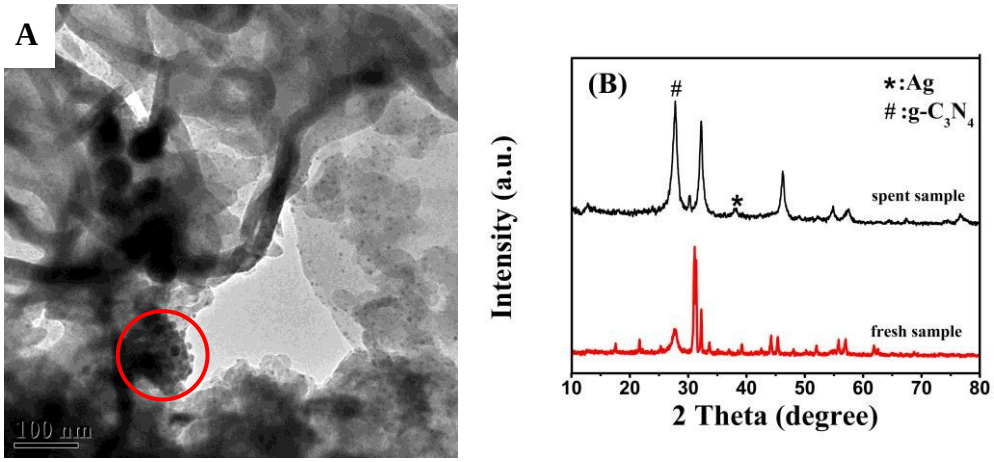

Fig. 9

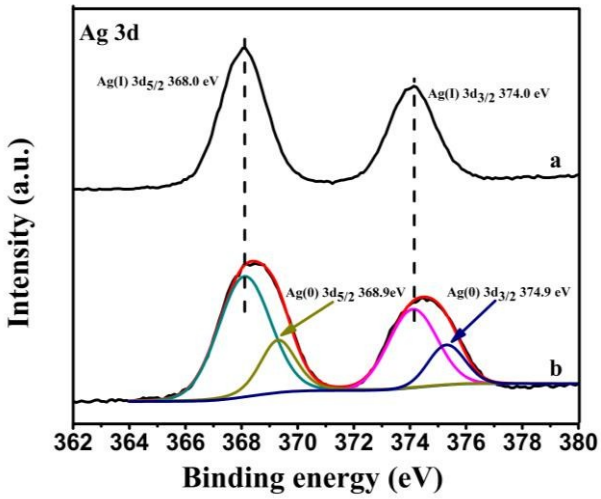

Fig. 10

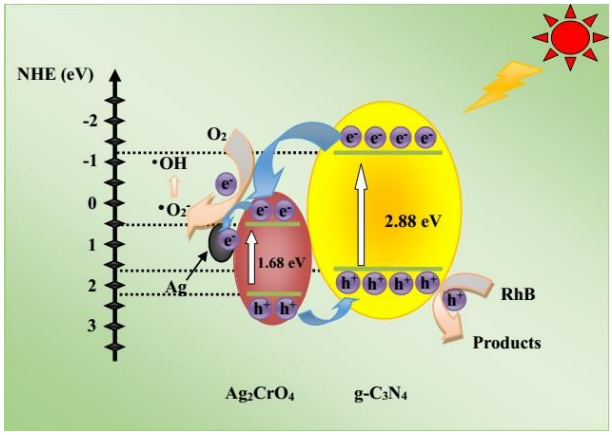

Fig. 11